Journal of Power Sources 196 (2011) 8383–8390

Contents lists available at ScienceDirect

Journal of Power Sources

journal homepage: www.elsevier.com/locate/jpowsour

The role of SiO_2 and sintering temperature on the grain boundary properties of $Ce_{0.8}Sm_{0.2}O_{2-\delta}$

D. Pérez-Coll[a,*], P. Núñez[b], J.R. Frade[c]

[a] Instituto de Cerámica y Vidrio (CSIC), Cantoblanco, 28049 Madrid, Spain
[b] Dep. Química Inorgánica, Universidad de La Laguna, 38200 La Laguna, Tenerife, Spain
[c] Dep. Engenharia Cerâmica e do Vidrio, CICECO Universidade de Aveiro, 3810-193 Aveiro, Portugal

ARTICLE INFO

Article history:
Received 30 March 2011
Received in revised form 6 June 2011
Accepted 22 June 2011
Available online 29 June 2011

Keywords:
Ceria
Silica
Impedance spectroscopy
Grain boundary
Electrolyte

ABSTRACT

The solid solution $Ce_{0.8}Sm_{0.2}O_{2-\delta}$ (20CSO) was synthesized by freeze-drying precursor procedure. Well-crystallized powders with nanometric grain sizes were obtained after calcining the precursor at 375 °C for 4 h. The effect of SiO_2-addition and sintering temperature on the properties of the bulk and grain boundary processes were studied. For this purpose, 20CSO–SiO_2 samples were prepared by the addition of 0.05 or 0.5 mol% SiO_2 to $Ce_{0.8}Sm_{0.2}O_{2-\delta}$, in the form of tetraethyl orthosilicate (TEOS). Also, 2 mol% Co was added to some of the precalcined compositions with and without silica-addition. Cobalt free samples were sintered at 1400, 1500 and 1600 °C and cobalt-added samples were sintered 1150 °C, for 10 h to obtain dense pellets. The electrical behaviour of the bulk was revealed to be nearly independent on sintering temperature and/or on the addition of impurities of SiO_2 and Co to the grain boundaries. This was explained by the low solubility of impurities in the grain fluorite structure. However, the grain boundary resistance showed important differences as function of sintering temperature and with the presence of impurities. The analysis of grain boundary properties suggests that segregated impurities affect the microstructure and also segregation of Sm at the space charge layer, thus changing both the specific grain boundary conductivity and microstructural parameters.

1. Introduction

Ceria-based materials have been widely studied for many years due to their potential application as solid electrolytes in several electrochemical devices as solid oxide fuel cells [1–4]. Their excellent conductivity compared to standard YSZ makes these electrolytes very attractive for use in the range 500–700 °C. However, ceria-based materials could be considerably affected by resistive grain boundaries, spoiling the overall conductivity even at intermediate temperature. This detrimental effect is more severe for low to moderate contents of aliovalent lanthanide additives, when the bulk conductivity is close to its maximum [5–7]. Some authors have attributed the grain boundary blocking effect in ceria- and zirconia-based materials to the presence of impurities [8–11], mainly SiO_2. Others explained its lower influence in samples with higher contents of trivalent lanthanide to the scavenger effect exerted by segregation of this additive [6]. Location of impurities is revealed as a crucial key to understand effects on grain boundary transport properties, pointing out to dependence on sintering temperature or other thermal treatments [10–12], and addition of several oxides [13–16] as usual ways to relocate impurities and/or produce scavenging reactions modifying specific properties of grain boundary conduction. However, highly resistive grain boundaries were reported even in high purity samples [17–19] suggesting prevailing space charge effects [18,20,21] on the intrinsic grain boundary properties. These evidences come out that, although the impurities could deteriorate the grain boundary conductivity, typical reduction in 2–3 orders of magnitude compared to the bulk conductivity is likely caused by intrinsic effects. Nevertheless, these effects could be easily tuned by the addition of minor contents of metal oxides as cobalt oxide and sintering at low temperature (~900–1150 °C), probably because the preferential segregation of this additive at grain boundaries suppresses the space-charge potential compared to samples fired at high temperatures (e.g. 1600 °C) without the sintering additive [22]. This points out the possible influence of external impurities in the solute segregation and thus in the space-charge layer and the specific grain boundary conductivity of ceria-based fluorite compounds.

In the present work the effect of external impurities and sintering temperature on the electrical behaviour of bulk and grain boundary properties of Sm-doped ceria were studied. The

* Corresponding author. Tel.: +34 917 355 840; fax: +34 917 355 843.
E-mail addresses: dpcoll@icv.csic.es, dpcoll@ull.es (D. Pérez-Coll).

0378-7753/$ – see front matter © 2011 Elsevier B.V. All rights reserved.
doi:10.1016/j.jpowsour.2011.06.075

solid solution $Ce_{0.8}Sm_{0.2}O_{2-\delta}$ was synthesized by freeze-drying. Two batches of powders were prepared after the addition of 0.05 and 0.5 mol% SiO_2 to $Ce_{0.8}Sm_{0.2}O_{2-\delta}$. Also 2 mol% Co was added to some of the powders with and without SiO_2-addition. The effect of SiO_2-addition was analyzed by impedance spectroscopy in air, including the use of different sintering temperatures to discriminate microstructural effects (constriction, grain size, grain boundary thickness) and specific properties (conductivity and permittivity) on the macroscopic behaviour (resistance and capacitance). Sintering temperature and composition of grain boundaries were revealed as important features in the modification of grain boundary behaviour, not only at microstructural level but also at specific level.

2. Experimental

Ceria–samaria powders with composition $Ce_{0.8}Sm_{0.2}O_{2-\delta}$ (20CSO) were prepared by freeze-drying precursor route previously reported [23]. Stoichiometric amounts of $Ce(NO_3)_3{\cdot}6H_2O$ (Aldrich, 99.99%) and $Sm(NO_3)_3{\cdot}6H_2O$ (Aldrich, 99.9%) were dissolved in distilled water, rapidly frozen by dropwise into liquid nitrogen and dehydrated in a freeze drier (Heto lyolab 3000) for 3 days. The obtained precursor was analyzed by thermogravimetry and differential thermal analysis (TG/DTA, PerkinElmer Pyris Diamond), subsequently calcined at 375 °C for 4 h and ground for 24 h in a home-made-YSZ ball milling. SiO_2-contaminated (0.05 or 0.5 mol% SiO_2) samples (20CSO0·05SiO_2 or 20CSO0·5SiO_2) were prepared by the addition of tetraethyl orthosilicate (TEOS) on pre-calcined 20CSO following a wet chemical method. For this purpose stoichiometric amounts of 20CSO and TEOS were mixed with distilled water, ethanol and hydrochloric acid to assure the precipitation of silica. The obtained paste was milled until dry in an agate mortar under an infrared light, calcined at 375 °C for 4 h and ball milled again. Cobalt-doped samples (2 mol% Co) were also prepared for both pure- and SiO_2-contaminated powders after adding an alcohol solution of $Co(NO_3)_2{\cdot}6H_2O$ (Panreac, purissimum) and milling until dry in a mortar. The resulting powders were then calcined at 650 °C for 1 h.

The as-prepared powders were studied by X-ray diffraction (XRD, Philips X'pert) to assess the fluorite single phase purity.

Cylindrical sintered pellets (~7.5–8 mm in diameter and ~1–1.5 mm in thickness) of samples without and with silica additions were prepared by uniaxially pressing the powders at 125 MPa in a 10 mm-diameter-die and sintering at 1400, 1500 and 1600 °C (cobalt-free samples) and 1150 °C (cobalt-added samples) for 10 h. Also some powders were heated at mentioned temperatures and XRD measurements and Rietveld refinement were performed. The values of apparent density of the samples were obtained by their mass and geometric volume and they were compared with the theoretical unit cell density values obtained by the crystallographic parameter. Scanning electron microscopy (SEM) and energy-dispersive X-ray spectroscopy (EDXS) were used to analyse the microstructure and locate the silica on thermally etched sintered bodies. The averaged grain sizes of the pellets were determined by lineal-interception method.

The bulk and grain boundary electrical properties of sintered pellets with Pt electrodes of 5.50 mm-diameter were studied by impedance spectroscopy in air by decreasing temperature from 1000 to 150 °C in the frequency range of 0.1–10^6 Hz.

3. Results

3.1. Thermal analysis

The TG/DTA results obtained from freeze-dried precursor show several steps of mass loss (Fig. 1). From room temperature to ~140 °C the mass loss may be caused by dehydration. In this range of temperature total loss is comprised by 3 steps of mass loss suggesting different processes of dehydration. The first step shows a peak in the DTA at 53 °C and produces a mass loss of 3.4%; this may be due to physisorbed water. Following water losses present two peaks in the DTA curve, one located at 87 °C and another one located at 135 °C, corresponding to crystallization water with a total mass loss of 14.3%. This sequential-dehydration-behaviour for crystallization water was previously observed [24,25] and was attributed to inequivalences in the water molecules around the metal ions. The main important mass loss (~36%) takes place from ~250 to 400 °C with an endothermic peak centered at 270 °C, which corresponds to the decomposition of nitrates [24,25]. Further weight loss of ~2% is observed for temperatures higher than 400 °C, possibly corresponding to decomposition of residual nitrates.

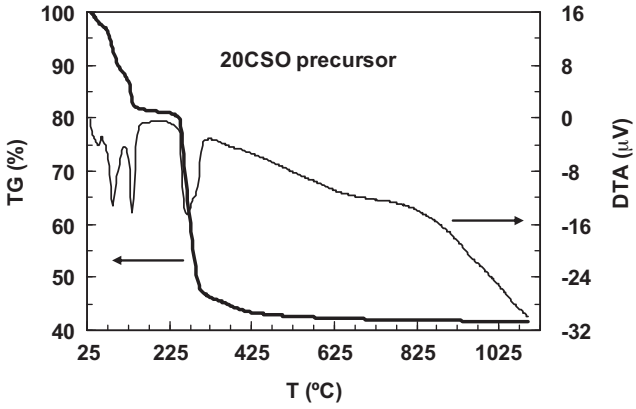

Fig. 1. TG/DTA measurements performed on freeze-dried precursor of $Ce_{0.8}Sm_{0.2}O_{1.9}$.

3.2. Structural and microstructural characterization

XRD data of powders calcined at 375 °C (for both pure and SiO_2-contaminated 20CSO samples) reveal the presence of fluorite single phases with wide diffraction peaks due to the nano size of crystallites. Also, the addition of cobalt after the synthesis of the fluorite does not produce the presence of any secondary phase in the XRD patterns. Powders heated at high temperature (1150–1600 °C) were also analyzed by XRD and the Rietveld refinement (Fig. 2) evidenced no appreciable changes in the unit cell parameter obtaining values ranging from 0.54343 to 0.54351 nm. This suggests that the possible dissolution of cobalt into the crystal structure is unappreciable when sintering temperature is low (1150 °C) and confirms the complete dissolution of Sm_2O_3 in CeO_2 in the studied range of sintering temperature. In the freeze-drying precursor route the diffusion of cations during the synthesis process takes place at atomic range given that each nanometric grain of the precursor preserves the stoichiometry of $Ce_{0.8}Sm_{0.2}O_{2-\delta}$-compound. This allows total incorporation of Sm^{3+} into the CeO_2 structure and high homogeneity at low temperature of synthesis (375 °C). A similar behaviour was observed for ceria-based materials prepared from other precursor routes as carbonate coprecipitation [26]. On the contrary, conventional solid state powder synthesis occurs at micrometric range as imposed by the precursors, and the expected $Ce_{0.8}Sm_{0.2}O_{2-\delta}$-composition may not reach homogeneity. The solid state reaction takes place between grains of different precursors, and complete dissolution of Ln^{3+} cations in the fluorite structure needs high heating temperatures [27]; this is also more likely to yield poorer homogeneity.

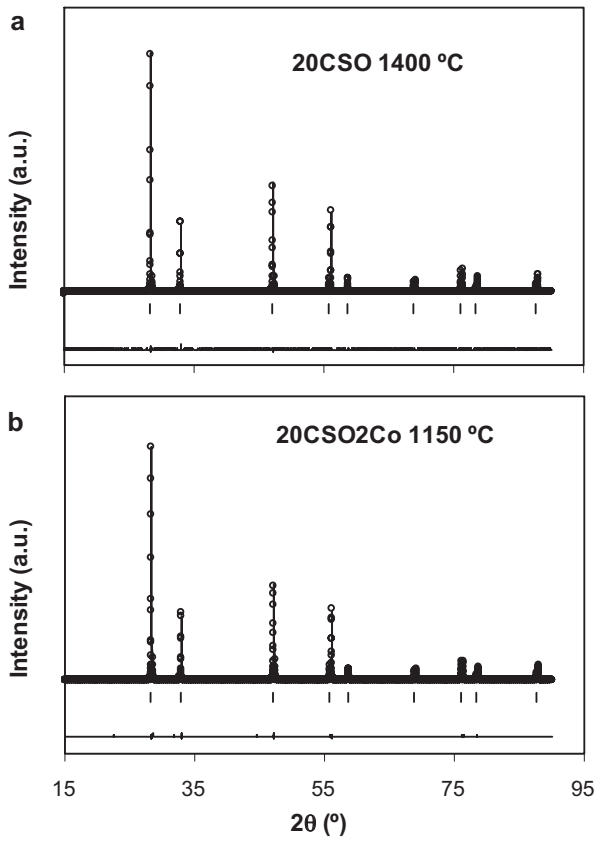

Fig. 2. XRD patterns and rietveld refinements of (a) 20CSO sample without additive sintered at 1400 °C and (b) 20CSO sample with 2 mol% Co sintered at 1150 °C.

Table 1 shows that the addition of cobalt enhances the densification of 20CSO at low temperature, as it was previously found for several compositions of ceria-based compounds [28–32], reaching a value of ~96% after sintering at 1150 °C, which is close to values obtained for cobalt-free samples sintered at 1400–1500 °C (~96–99% of the theoretical density). A lower sinterability was observed in 20CSO0·5SiO_2 samples, which show lower densification with ~86% after sintering at 1400 °C; this suggests the presence of non-negligible SiO_2 layer distributed along the grain boundary with negative impact on mass transport. Moreover, presence of silica also affects the sinterability of cobalt-added samples, and their densification remains in the order of ~90–92% after firing at 1150 °C. SiO_2-samples sintered at higher temperature (≥1500 °C) reach good densification without addition of cobalt (~95–99%). Table 1 also shows that there is a sharp increase in grain size for sintering temperatures higher than 1400 °C. A previous study of the densification behaviour of $Ce_{0.9}Gd_{0.1}O_{1.95}$ as function of sintering temperature [33] revealed the presence of two regimes in the entire sintering process. In the first stage, densification occurs without important changes in grain size, whereas grain growth takes place in the second stage. Current results indicate that 20CSO samples are in the grain growth regime for temperatures higher than 1400 °C, i.e. at temperatures required to reach high densification. On the other hand, the introduction of impurities of SiO_2 in 20CSO samples affects densification and hinders grain growth at identical temperatures, as shown in Table 1. This is probably due to preferential segregation of silica at grain boundaries and its effect on grain boundary motion, as suggested by the presence of silica rich precipitates (marked with arrows in Fig. 3). The sharp edge shape of silica rich grains suggest that precipitation took place during thermal etching, preferentially at multiple grain contacts, and most probably corresponding to the location of highest concentration of this contaminant. The addition of cobalt retains the submicrometric grain size for SiO_2-loaded samples and for samples without SiO_2-addition after sintering at 1150 °C due to the slow diffusion at this temperature.

3.3. Electrical properties

Fig. 4 shows impedance spectra obtained at 250 °C for 20CSO and 20CSO0·5SiO_2 samples sintered at different temperatures. All the spectra reveal the presence of three deconvoluted contributions due to differences in orders of magnitude of the relaxation frequency of each process. The high-frequency arc, associated to the bulk contribution, is mainly independent of sintering temperature and/or of the addition of SiO_2 and Co after the synthesis of the powders. Fig. 5 shows the Arrhenius representation of the bulk conductivity for samples sintered at different temperatures in the entire range of measuring temperature. The values of bulk resistance at high temperature were estimated by the linear extrapolation of the grain boundary resistance to the high temperature regime and the experimental values of total resistance [22]. The activation energy of the bulk process at low temperature (150–400 °C) is in the range 0.85–0.89 eV (Table 1), with no appreciable dependence on sintering conditions and additions of SiO_2 and/or Co. At high temperatures the activation energy decreases considerably to values of 0.51–0.62 eV, as defect association becomes weaker, with a considerably uncertainty due to gradual transition between the low and high temperature regimes. It is apparent from Fig. 5 that the composition of bulk and the asso-

Table 1
Relative density (R.D.), average grain size (d_g), activation energy of the bulk in the low temperature regime ($E_{aB\text{-}LT}$), activation energy of the bulk in the high temperature regime ($E_{aB\text{-}HT}$) and activation energy of the grain boundary (E_{aGB}), for samples with and without SiO_2-addition sintered at 1150–1600 °C. Note that samples sintered at 1150 °C were previously loaded with 2 mol% Co.

Sample	T_s (°C)	R.D. (%)	d_g (μm)	$E_{aB\text{-}LT}$ (eV)	$E_{aB\text{-}HT}$ (eV)	E_{aGB} (eV)
20CSO + 2%Co	1150	96	0.84	0.88	0.62	0.98
20CSO	1400	96	1.03	0.89	0.57	0.98
20CSO	1500	99	2.57	0.88	0.62	0.97
20CSO + 0.05%SiO_2 + 2%Co	1150	92	0.6	0.85	0.51	1.00
20CSO + 0.05%SiO_2	1400	96	1.1	0.86	0.54	1.00
20CSO + 0.05%SiO_2	1500	98	2.9	0.86	0.56	1.00
20CSO + 0.05%SiO_2	1600	99	4.9	0.86	0.57	0.98
20CSO + 0.5%SiO_2 + 2%Co	1150	90	0.40	0.86	0.52	1.00
20CSO + 0.5%SiO_2	1400	86	0.65	0.87	0.54	0.99
20CSO + 0.5%SiO_2	1500	95	2.0	0.86	0.61	0.98
20CSO + 0.5%SiO_2	1600	98	4.0	0.86	0.57	0.99

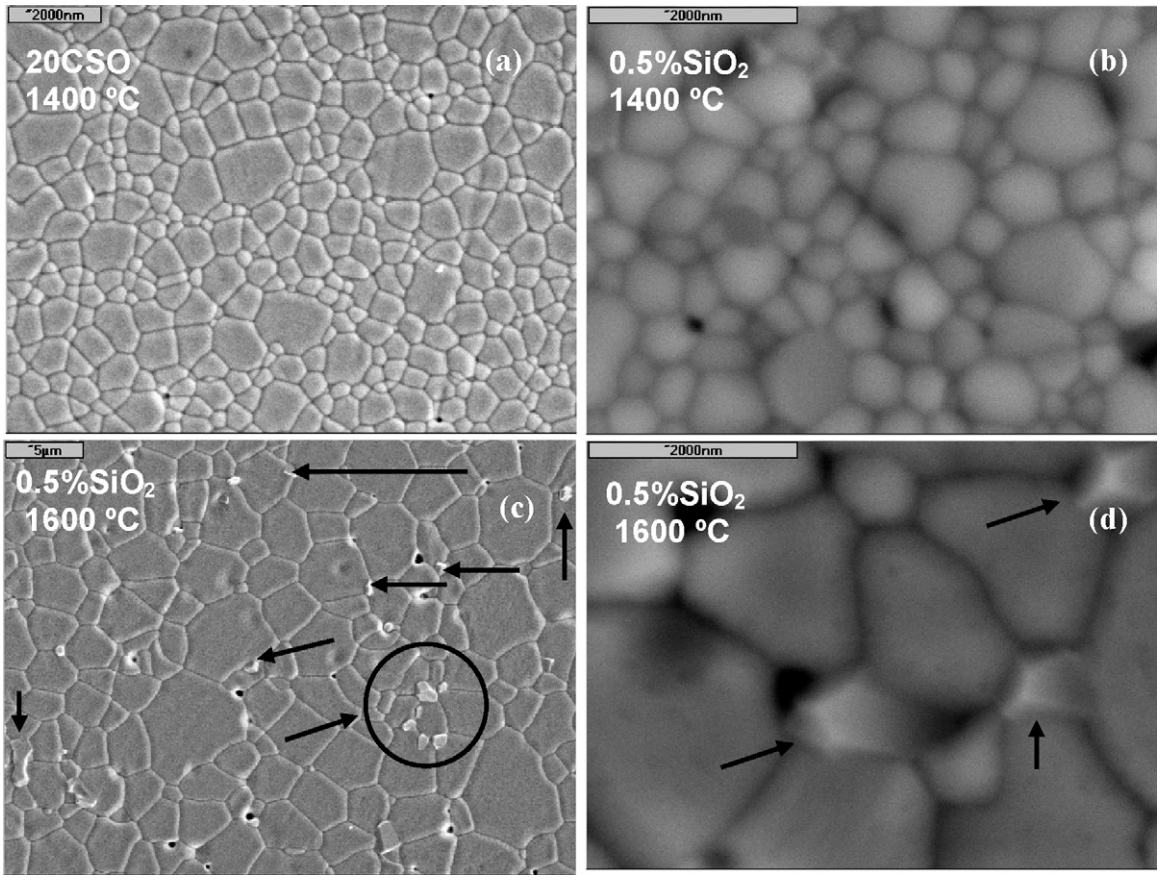

Fig. 3. SEM images of 20CSO sample sintered at 1400 °C (a) and 0.5%SiO_2-contaminated–20CSO sintered at 1400 °C (b) and 1600 °C (c) and (d).

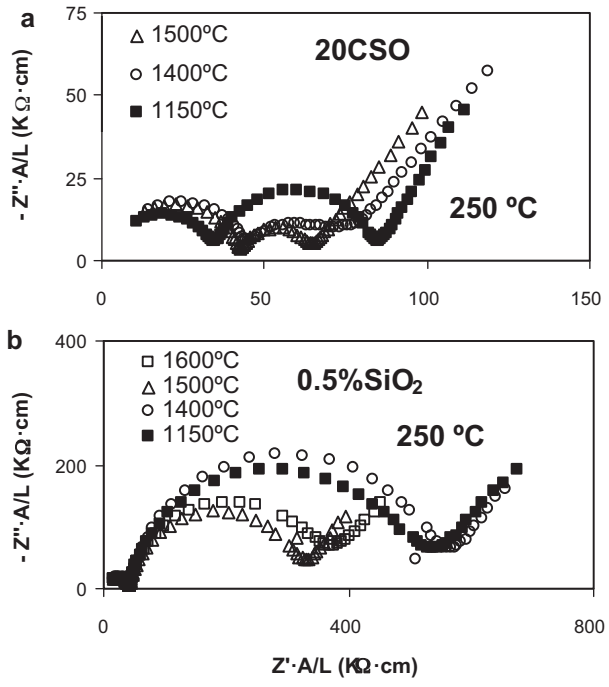

Fig. 4. Impedance spectra obtained at 250 °C for samples sintered at different temperatures, (a) 20CSO samples without SiO_2-addition and (b) 0.5% SiO_2-loaded samples. Cobalt addition was carried out in both pure and SiO_2-contaminated samples sintered at 1150 °C.

ciation of defects are independent on the sintering conditions in the studied range of temperature. Also, it suggests that the dissolution of SiO_2 and/or Co in the lattice is invaluable as it was argued in the previous analysis of the XRD data.

On the other hand, major differences were observed in the intermediate-frequency arc, associated with the grain boundary process (Fig. 4). In a previous work we found that 20CSO sample sintered at 1600 °C possessed a large grain boundary arc, which was clearly decreased with the addition of cobalt and sintering at 1150 °C [22]. However, current results show that the arc associated to grain boundaries in the cobalt-added sample is still higher than for samples without cobalt addition sintered at 1400 and 1500 °C. This can be related to the expected dependence of grain boundary properties on average grain size. Following the classical brick layer model [18,34,35] the grain boundary resistance (R_{gb}) and capacitance (C_{gb}) could be expressed as:

$$R_{gb} = \rho_{gb}\left(\frac{L}{A}\right)\left(\frac{\delta_{gb}}{d_g}\right) \quad (1)$$

$$C_{gb} = \varepsilon_0\varepsilon_{rgb}\left(\frac{A}{L}\right)\left(\frac{d_g}{\delta_{gb}}\right) \quad (2)$$

where ρ_{gb} and ε_{rgb} are the resistivity and permittivity of the grain boundary process; ε_0 is the permittiviy of free space; L is the thickness of the sample; A is the area of the electrodes, and δ_{gb} and d_g are the average values of grain boundary thickness and grain size, respectively. According to Eq. (1), samples with higher grain sizes should possess lower grain boundary contribution to the total resistance due to the decrease in the number of effective interfaces. This

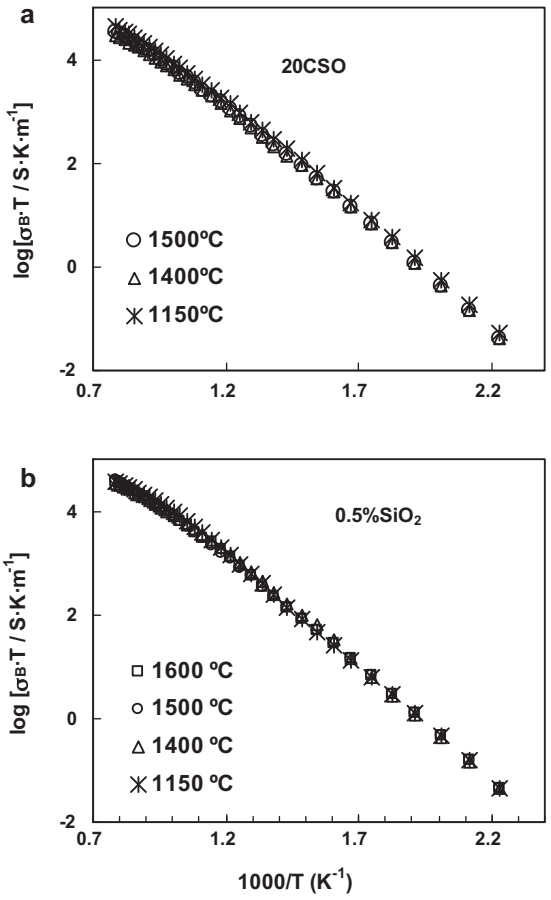

Fig. 5. Arrhenius representation of the bulk conductivity of samples sintered at different temperatures for (a) 20CSO and (b) 20CSO + 0.5%SiO_2 (note that 2%Co was added to the precalcined powders before sintering at 1150 °C).

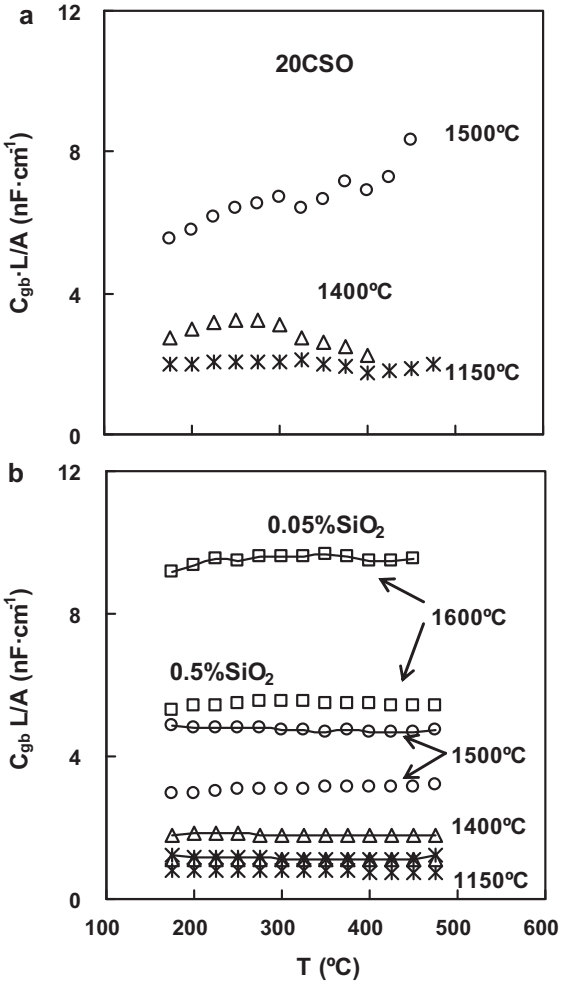

Fig. 7. Geometrically normalized grain boundary capacitance as function of measuring temperature for samples sintered at 1600 (squares), 1500 (circles), 1400 (triangles) and 1150 °C (crosses) for (a) 20CSO and (b) 20CSO + 0.05%SiO_2 (points joined with lines) and 20CSO + 0.5%SiO_2 (single points). Samples sintered at 1150 °C were previously doped with 2 mol%Co.

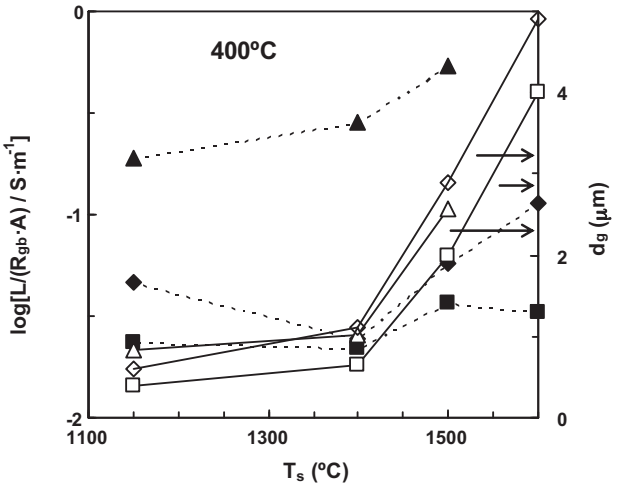

Fig. 6. Geometrically normalized grain boundary conductance (closed symbols) and average grain size (open symbols) as function of sintering temperature for samples without silica-addition and for silica-added-samples. Samples sintered at 1150 °C were previously doped with 2 mol%Co. Triangles are for samples without silica-addition, diamonds for 0.05% SiO_2-added, and squares are for 0.5% SiO_2-added.

trend is nearly observed for 20CSO samples sintered between 1150 and 1500 °C (Fig. 6).

Contamination with silica produces a large increase in the intermediate frequency arc of the impedance spectra at each sintering temperature (Fig. 4(b)), compared to 20CSO, which corresponds to apparent decrease of the geometrically normalized grain boundary conductance ($LA^{-1}R_{gb}{}^{-1}$) (Fig. 6).

The identification of specific transport properties and the microstructural effects are essential to obtain a correct interpretation of the macroscopic values of grain boundary resistance and capacitance. Figs. 4 and 6 show that the introduction of SiO_2 spoils the grain boundary properties but its nature should be carefully analyzed. Furthermore, the grain boundary capacitance also depends on processing, as shown in Fig. 7, for geometrically normalized grain boundary capacitance ($C_{gb}LA^{-1}$). These results can be correlated mostly to the increase in grain size (Table 1), with corresponding increase in capacitance of the samples, according to the mentioned brick layer model (Eq. (2)). However, this is insufficient to explain important differences of grain boundary capacitance results for samples with and without SiO_2-addition, which are still reflected in a decrease of ~50% of the values of capacitance at each sintering temperature after the addition of 0.5% SiO_2.

One will proceed with a simple modification of the brick layer model to take into account combinations of changes in specific grain boundary properties, changes in average grain sizes, and possibly also other less obvious changes at grain boundary level, resulting in local constrictions [36]; this is described on assuming a constriction factor ($f_{cons} \leq 1$) to account for effective changes in area

to thickness ratio for electrical conduction across grain boundaries, that is:

$$\left(\frac{A}{L}\right)_{\text{eff}} = (1 - f_{\text{cons}})\frac{A}{L} \tag{3}$$

Note that the effective geometric factor $(A/L)_{\text{eff}}$ equals the measured A/L in the case of samples without constriction ($f_{\text{cons}} = 0$), i.e., the so-called constriction factor f_{cons} is a measure of how severe is the constriction effects on grain boundary properties. The mechanism of conduction of the proposed model could be described by two parallel paths for conduction at grain boundaries through clean grain to grain contacts and through the silica-rich. This revised model allows one to obtain general expressions for grain boundary resistance and capacitance according to:

$$\frac{L}{R_{\text{gb}}Ad_{\text{g}}} = \frac{\sigma_{\text{gb1}}(1 - f_{\text{cons}})}{\delta_1} + \frac{\sigma_{\text{gb2}}f_{\text{cons}}}{\delta_2} = \frac{\sigma_{\text{gb1}}(1 - f_{\text{cons}})}{\delta_1}\left[1 + \frac{\sigma_{\text{gb2}}f_{\text{cons}}\delta_1}{\sigma_{\text{gb1}}(1 - f_{\text{cons}})\delta_2}\right] \tag{4}$$

$$\frac{C_{\text{gb}}L}{Ad_{\text{g}}} = \varepsilon_0\varepsilon_{r1}\frac{(1 - f_{\text{cons}})}{\delta_1}\left[1 + \frac{\varepsilon_{\text{r2}}f_{\text{cons}}\delta_1}{\varepsilon_{\text{r1}}(1 - f_{\text{cons}})\delta_2}\right] \tag{5}$$

where σ_{gb1} and σ_{gb2} are the specific grain boundary conductivity corresponding to transport along clean grain contacts and through the silica-rich layer, respectively; ε_{r1} and ε_{r2} are the corresponding relative permittivities, δ_1 and δ_2 their thicknesses. Given that the resistivity of the silica-rich layer is much higher than that of the clean-grain contacts, the diffusion of ions nearly reduces to the path of clean contacts [35]. On the other hand, the expected lower values of permittivity of silica-based phases, higher thickness relative to silica-clean space charge regions (i.e. $\delta_2 > \delta_1$) and possibly also moderate levels of constriction also allows one to assume that the grain boundary capacitance is only affected by the permittivity of clean interfaces. These assumptions simplify considerably the expressions describing resistance and capacitance as follows:

$$\frac{L}{R_{\text{gb}}Ad_{\text{g}}} \approx \frac{\sigma_{\text{gb1}}(1 - f_{\text{cons}})}{\delta_1} \tag{6}$$

$$\frac{C_{\text{gb}}L}{Ad_{\text{g}}} \approx \varepsilon_0\varepsilon_{\text{r1}}\frac{(1 - f_{\text{cons}})}{\delta_1} \tag{7}$$

Under these circumstances, the angular relaxation frequency should still remain nearly independent of the constriction factor, except for cases when specific properties also change, i.e.:

$$\omega_{\text{gb}} = (C_{\text{gb}}R_{\text{gb}})^{-1} \approx \frac{\sigma_{\text{gb1}}}{\varepsilon_0\varepsilon_{\text{r1}}} \tag{8}$$

Fig. 8 shows an alternative Arrhenius representation of the normalized grain boundary resistance after the introduction of the average grain size of the samples ($R_{\text{gb}}Ad_{\text{g}}/L$), according to Eq. (6). Fig. 8(a) shows that differences in grain boundary behaviour for samples without SiO_2 addition sintered between 1150 and 1500 °C can be ascribed mainly to differences in grain size. On the other hand, the study performed on SiO_2-loaded samples (with 0.5% SiO_2) shows clearly different behaviour in which the factor $R_{\text{gb}}Ad_{\text{g}}/L$ increases systematically with the increase in sintering temperature. This may be ascribed to either decreasing specific grain boundary conductivity, or increasing role played by constrictions, because increase in average grain size corresponds to decrease in grain boundary interfaces and, thus, increasing concentration of impurities. One also sees negative effects for 0.05% SiO_2 (Fig. 8(b)), including effects on samples obtained at 1150 °C with cobalt addition. However, results obtained for samples sintered at 1400–1500 °C converge in a nearly common Arrhenius line, which suggests that constrictions are unlikely to play a significant effect

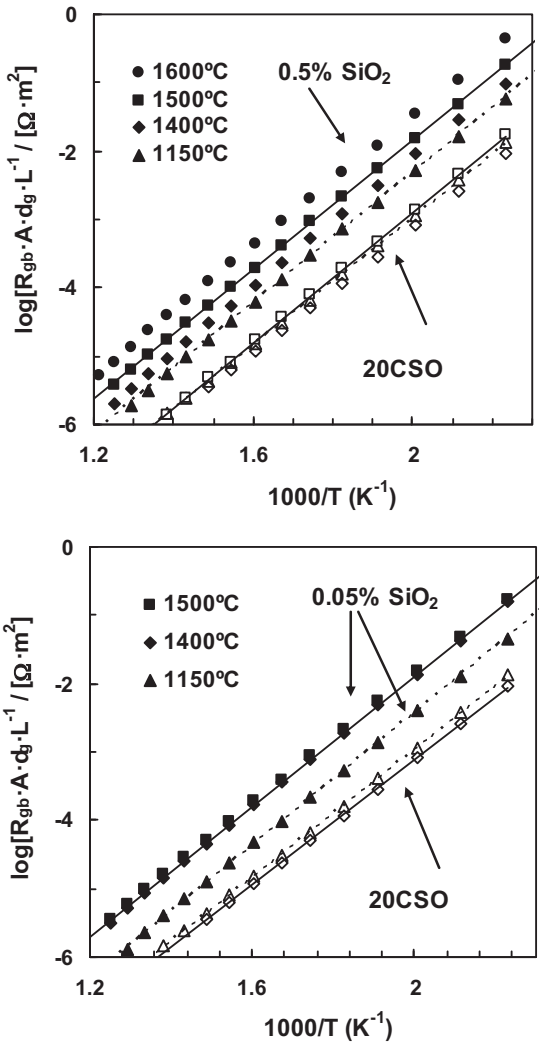

Fig. 8. Arrhenius representation of the normalized grain boundary resistance of samples sintered at different temperatures after correction for differences in average grain size. Open symbols are for samples without silica-addition, and corresponding closed symbols are for 0.5% SiO_2 (a) or 0.05% SiO_2 (b). Samples sintered at 1150 °C were previously doped with 2 mol%Co.

for silica additions up to about 0.05 mol%. In this case, changes in specific properties may be related to space charge effects exerted by different combinations of segregated species (i.e., silica, cobalt oxide or both).

The grain boundary capacitance provides additional information after accounting for geometric changes and also changes in grain size. For this purpose the factor $C_{\text{gb}}L/(Ad_{\text{g}})$ is represented as function of measuring temperature in Fig. 9. Contrary to results for grain-size normalized conductance presented in Fig. 8, the results of grain size-normalized capacitance (Fig. 9) lay in a much narrower range for samples sintered at different temperatures. Note that higher scattering is observed for samples without addition of silica, probably because de-convolution of impedance spectra yields poorer fitting, due to partial overlapping of the grain boundary and electrode arcs (see Fig. 4(a)). Nevertheless, the grain size normalized results obtained for samples heavily contaminated with silica still show important dependence on sintering conditions, and are clearly lower than for clean samples.

Eq. (8) also allows one to determine the specific grain boundary conductivity (σ_{gb}) by means of the angular relaxation frequency of the process, under the usual assumption that the permittivity

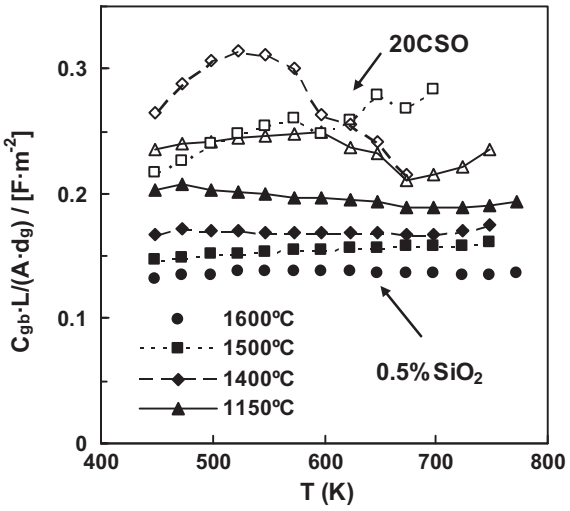

Fig. 9. Alternative representation of normalized grain boundary capacitance after correction for differences in average grain size. Open symbols are for samples without silica-addition and closed symbols for 0.5% SiO_2-added samples.

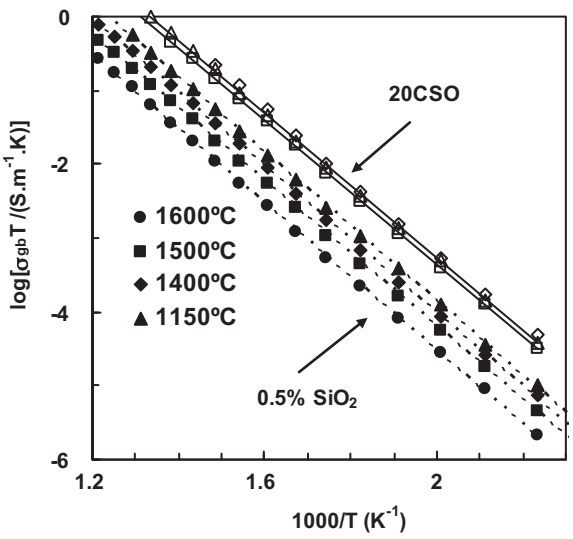

Fig. 10. Arrhenius representation of the specific grain boundary conductivity for samples without addition of silica (open symbols) and for samples with 0.5% SiO_2-addition (closed symbols).

of the bulk equals that of the grain boundary ($\varepsilon_{rB} \approx \varepsilon_{rgb} \approx \varepsilon_r$) [20], according to [37]:

$$\sigma_{gb} = \omega_{gb} \cdot \varepsilon_0 \cdot \varepsilon_r \quad (9)$$

Though permittivity should be determined from the capacitance of the bulk ($\varepsilon_r \approx C_B L/(A\varepsilon_0)$), the actual value of capacitance of ceria based samples with commonly used pellet configuration is of the same order of magnitude of stray effects imposed by the experimental equipment used for impedance spectroscopy measurements; this hinders the determination of an accurate value of permittivity. Different experimental procedures, as the use of an external auxiliary resistance [38] or the analysis of the variation of the capacitance as function of A/L [22], could be used to estimate the value of the stray capacitance introduced by the equipment. In previous works [33,38,39] we have obtained values of permittivity in the range $\varepsilon_r \approx 28$–36 for samaria- and gadolinia-doped ceria, which are in good agreement with previously reported values for cerias with very high values of A/L [40]. Due to the observed low dependence of permittivity of ceria- and zirconia-based materials on compositional changes [35], we have assumed a constant value of $\varepsilon_r = 30$ in the estimation of the specific grain boundary conductivity.

Fig. 10 also suggests that results obtained for uncontaminated 20CSO converge to nearly common trends, for sintering temperatures in the range 1150–1500 °C, whereas heavily contaminated samples show poorer results and important changes with sintering temperature. Results reported in literature suggest that specific grain boundary conductivity often becomes poorer with increase in average grain size, originated by corresponding increase in sintering temperature [18,40–42], and such effects are usually ascribed to increase in space charge potential [35,41,42]. However, the most pronounced decrease in specific grain boundary conductivity often occurs for samples with submicrometer grain sizes. In addition, differences between results obtained for ceria-based samples sintered at relatively low and high sintering temperatures could also be dependent on segregation of cobalt used as sintering aid [22,43]. In a very recent work [39] one also showed that the specific grain boundary conductivity obtained for $Ce_{0.9}Gd_{0.1}O_{1.95}$ samples prepared by "Spark Plasma Sintering" with an average grain size of ~120 nm were similar to those obtained for a ceramic sample with average grain size of ~2.2 μm, sintered at 1500 °C by conventional method. Moreover, $Ce_{0.9}Gd_{0.1}O_{1.95}$ samples sintered with the conventional procedure between 1225 and 1500 °C, presented

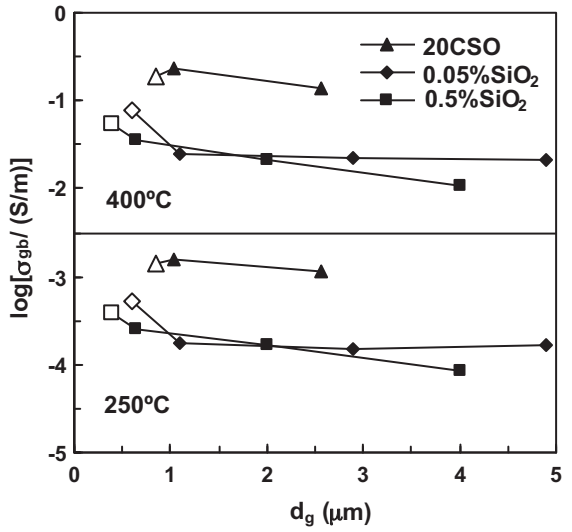

Fig. 11. Dependence of specific grain boundary conductivity on grain size, for samples without addition of silica (triangles), for 0.05% SiO_2 (diamonds) and for 0.5% SiO_2 (squares), at 250 °C and 400 °C. The open symbols indicate samples sintered at 1150 °C with addition of cobalt.

similar values of specific grain boundary conductivity in spite of possessing large differences in grain size, ~0.17–1.87 μm, and relative density ~76–99% [33]. Thus, the results in Fig. 10 still suggest significantly stronger effects of sintering temperature on specific grain boundary properties for samples contaminated with silica.

This may also be ascribed to the corresponding dependence on grain size, as shown in Fig. 11. Indeed, this does not exclude significant constriction effects for heavily contaminated samples, as emphasized by corresponding changes in grain boundary capacitance normalized for changes in average grain size (Fig. 9). Fig. 11 also shows clear evidence that cobalt additions (open symbols) partially opposes the negative impact of silica on specific grain boundary conductivity.

Fig. 11 also shows greater dependence on grain size for heavily contaminated samples (with 0.5% SiO_2), and negligible dependence for samples with 0.05% SiO_2, except for simultaneous addition of cobalt. In this case, one cannot exclude possible indirect constric-

tion effects on specific properties, as predicted on combining Eqs. (4) and (5), without further assumptions; this yields:

$$\omega_{gb} = \frac{\sigma_{gb1}}{\varepsilon_{r1}\varepsilon_0} \cdot \frac{1 - f_{cons} + f_{cons}((\sigma_{gb2}\delta_1)/(\sigma_{gb1}\delta_2))}{1 - f_{cons} + f_{cons}((\varepsilon_{r2}\delta_1)/(\varepsilon_{r1}\delta_2))} \quad (10)$$

Since grain growth corresponds to decreasing area of grain boundaries ($A_{gb} \propto 1/d_g$), redistribution of silica should yield the following dependence of constriction factor on silica content and average grain size:

$$f_{cons} \propto \%SiO_2 \cdot d_g \quad (11)$$

This may still explain the greater dependence on average grain size for high silica contents, shown in Fig. 11.

It is also noticeable that the values of grain boundary activation energy are in the range 0.98–1.00 eV without apparent modification with the sintering temperature, and also that these values fit very well with the values obtained for samples without addition of SiO_2 (Table 1). Similar values of activation energy suggest similar conduction process of ions through the grain boundaries, even though the composition, nature, viscosity and location of impurities are highly dependent on sintering conditions [9,35,44–46]. This is consistent with most of evidences reported by other researchers [35,40,46,47] suggesting that the transport of ions at grain boundaries in SiO_2-contaminated fluorites takes place in direct contacts between clean grains, i.e., grain boundaries are only partially wetted by silica, decreasing the contact area between grains, without changing the nature of conduction. Note that if the impurity-phase were continuous, the activation energy of grain boundary contribution should be different from that obtained for clean grain boundaries [35,46], and dependent on the nature of conduction in the glassy phase, thus being affected by sintering temperature. Thus, increase of grain boundary resistance of heavily contaminated samples (Fig. 6) may be mainly due to the fact that a significant fraction of internal interfaces is blocked by the poorly conducting SiO_2-rich phase, thus hindering oxygen ion migration.

4. Conclusions

The grain boundary behaviour of ceria–samaria materials is clearly affected by silica, even for moderate contamination (0.05 mol%), without significant effects on intragrain (bulk) properties. These effects are clearly dependent on sintering conditions, mainly due to effects on average grain size, level of contamination, and also presence of cobalt added as sintering aid. For moderate contamination by silica one expects prevailing effects on specific grain boundary properties rather than constriction effects. Specific grain boundary properties are still strongly affected by moderate contamination by silica. Simultaneous addition of cobalt as sintering aid plays a positive role, probably by interacting with silica. For heavily contaminated samples (with 0.5% SiO_2) one found evidence of coexisting effects on specific grain boundary properties and constriction effects, especially for the highest sintering temperatures. Dependence of constriction effects can be ascribed to increase in average grain size and corresponding redistribution of the silica in the shrinking grain boundary area.

Acknowledgements

This work was sponsored by MCINN in Spain (ENE2009-14750-C05-03). D. Pérez-Coll is also grateful to MCINN and ICV-CSIC for a "Ramón y Cajal" contract. The authors are also acknowledged to J.C.C. Abrantes (ESTG-IPVC, Viana do Castelo, Portugal) for the use of the Estereologia-Software Package employed to determine the averaged grain size of the samples.

References

[1] B.C.H. Steele, J. Mater. Sci. 36 (2001) 1053.
[2] J.A. Kilner, Solid State Ionics 8 (1983) 201.
[3] H. Inaba, H. Tagawa, Solid State Ionics 83 (1996) 1.
[4] M. Mogensen, N.M. Sammes, G.A. Tompsett, Solid State Ionics 129 (2000) 63.
[5] Z. Zhan, T.-L. Wen, H. Tu, Z.-Y. Lu, J. Electrochem. Soc. 148 (5) (2001) A427.
[6] T.S. Zhang, J. Ma, S.H. Chan, P. Hing, J.A. Kilner, Solid State Sci. 6 (2004) 565.
[7] T.S. Zhang, J. Ma, H.T. Huang, P. Hing, Z.T. Xia, S.H. Chan, J.A. Kilner, Solid State Sci. 5 (2003) 150.
[8] J.E. Bauerle, J. Phys. Chem. Solids 30 (1969) 2657.
[9] A.E. Hughes, B.A. Sexton, J. Mater. Sci. 24 (1989) 1057.
[10] S.P.S. Badwal, J. Drennan, Solid State Ionics 40 (1990) 869.
[11] J.-H. Lee, T. Mori, J.-G. Li, T. Ikegami, M. Komatsu, H. Haneda, J. Electrochem. Soc. 147 (2000) 2822.
[12] D.-S. Kim, P.-S. Cho, J.-H. Lee, D.-Y. Kim, S.B. Lee, Solid State Ionics 177 (19–26) (2006) 2125.
[13] T.S. Zhang, J. Ma, Y.J. Leng, S.H. Chan, P. Hing, J.A. Kilner, Solid State Ionics 168 (2004) 187.
[14] Y.H. Cho, P.-S. Cho, G. Auchterlonie, D.K. Kim, J.-H. Lee, D.-Y. Kim, H.-M. Park, J. Drennan, Acta Mater. 55 (2007) 4807.
[15] G.S. Lewis, A. Atkinson, B.C.H. Steele, in: U. Bossel (Ed.), Proceeding of 4th European SOFC Forum, vol. 2, Oberrohrdorf, Switzerland, 2000, p. 773.
[16] J.A. Lane, J.L. Neff, G.M. Christie, Solid State Ionics 177 (2006) 1911.
[17] M. Aoki, Y.M. Chiang, I. Kosacki, I.J.R. Lee, H.L. Tuller, Y.P. Liu, J. Am. Ceram. Soc. 79 (1996) 1169.
[18] M.J. Verkerk, B.J. Middelhuis, A.J. Burggraaf, Solid State Ionics 6 (1982) 159.
[19] X. Guo, W. Sigle, J. Maier, J. Am. Ceram. Soc. 86 (2003) 77.
[20] X. Guo, J. Maier, J. Electrochem. Soc. 148 (3) (2001) E121.
[21] X. Guo, Y. Ding, J. Electrochem. Soc. 151 (2004) J1.
[22] D. Pérez-Coll, P. Núñez, J.R. Frade, J. Electrochem. Soc. 153 (3) (2006) A478.
[23] D. Pérez-Coll, P. Núñez, J.R. Frade, J.C.C. Abrantes, Electrochim. Acta 48 (2003) 1551.
[24] M. Kamruddin, P.K. Ajikumar, R. Nithya, A.K. Tyagi, B. Raj, Scr. Mater. 50 (2004) 417.
[25] M. Kamruddin, P.K. Ajikumar, R. Nithya, G. Mangamma, A.K. Tyagi, B. Raj, Powder Technol. 161 (2006) 145.
[26] T.S. Zhang, J. Ma, L.H. Luo, S.H. Chan, J. Alloys Compd. 422 (1–2) (2006) 46.
[27] T.S. Zhang, J. Ma, L.B. Kong, P. Hing, H. Chan, J.A. Kilner, Electrochem. Solid State Lett. 7 (6) (2004) J13.
[28] C. Kleinlogel, L.J. Gauckler, Solid State Ionics 135 (2000) 567.
[29] T. Zhang, P. Hing, H. Huang, J. Kilner, J. Eur. Ceram. Soc. 22 (2002) 27.
[30] E. Jud, Z. Zhang, W. Sigle, L.J. Gauckler, J. Electroceram. 16 (2006) 191.
[31] D. Pérez-Coll, J.C. Ruiz-Morales, D. Marrero-López, P. Núñez, J.R. Frade, J. Alloys Compd. 467 (2009) 533.
[32] D.P. Fagg, S. García-Martín, V.V. Kharton, J.R. Frade, Chem. Mater. 21 (2) (2009) 381.
[33] D. Pérez-Coll, E. Sánchez-López, G.C. Mather, Solid State Ionics 181 (21–22) (2010) 1033.
[34] J.C.C. Abrantes, J.A. Labrincha, J.R. Frade, J. Eur. Ceram. Soc. 20 (2000) 1603.
[35] X. Guo, R. Waser, Prog. Mater. Sci. 51 (2006) 151.
[36] M.C. Steil, F. Thevenot, M. Kleitz, J. Electrochem. Soc. 144 (1997) 390.
[37] E. Chinarro, J.R. Jurado, F.M. Figueiredo, J.R. Frade, Solid State Ionics 160 (2003) 161.
[38] A.A.L. Ferreira, A.L. Horovistiz, J.C.C. Abrantes, D. Pérez-Coll, P. Núñez, J.R. Frade, Mater. Res. Bull. 44 (2009) 884.
[39] D. Pérez-Coll, G.C. Mather, Solid State Ionics 181 (2010) 20.
[40] G.M. Christie, F.P.F. van Berkel, Solid State Ionics 83 (1996) 17.
[41] X. Guo, Z. Zhang, Acta Mater. 51 (2003) 2539.
[42] C. Sánchez-Bautista, A.J. Dos Santos-García, J. Peña-Martínez, J. Canales-Vázquez, Solid State Ionics 181 (2010) 1665.
[43] D. Pérez-Coll, P. Núñez, J.C. Ruiz-Morales, J. Peña-Martínez, J.R. Frade, Electrochim. Acta 52 (2007) 2001.
[44] S. Kobayashi, J. Mater. Sci. Lett. 4 (1985) 268.
[45] S.P.S. Badwal, Appl. Phys. A 50 (1990) 449.
[46] S.P.S. Badwal, Solid State Ionics 76 (1995) 67.
[47] M.C. Martin, M.L. Mecartney, Solid State Ionics 161 (2003) 67.